Characterizing flow zones in a fractured and karstified limestone aquifer through integrated interpretation of geophysical and hydraulic data

6 authors, including:

N. Van Meir
Vrije Universiteit Brussel
37 PUBLICATIONS **182** CITATIONS

SEE PROFILE

David Jaeggi
Swisspep Institute For Quality And Research In Healthcare
23 PUBLICATIONS **131** CITATIONS

SEE PROFILE

Simon Loew
ETH Zurich
254 PUBLICATIONS **1,774** CITATIONS

SEE PROFILE

Philippe Adrien Pezard
French National Centre for Scientific Research
190 PUBLICATIONS **2,384** CITATIONS

SEE PROFILE

Some of the authors of this publication are also working on these related projects:

Geological processes and measurement methods influencing the depth distribution of permeabilities in crystalline rocks View project

Mechanics of macroscopic fracture development in sub-critically stressed rock under near-surface environmental conditions View project

Characterizing flow zones in a fractured and karstified limestone aquifer through integrated interpretation of geophysical and hydraulic data

Nathalie Van Meir · David Jaeggi · Martin Herfort ·
Simon Loew · Philippe A. Pezard · Gérard Lods

Abstract A detailed and integrated geologic–hydraulic–geophysical–geochemical study of groundwater flow in the near-vicinity of a borehole drilled into fractured and karstified limestone demonstrates the power of such an integrated approach in localising and characterising preferential groundwater flow pathways and ambient borehole flow. The study, conducted in the vicinity of a 100-m-deep research borehole on the island of Mallorca, achieves such characterisation on a scale from millimetres to tens of metres in scale. More specifically, it adds single packer and open-hole pumping test interpretations to the results obtained during fluid logging, impeller flowmeter testing, borehole imaging, core descriptions and an innovative fracture analysis. This approach allows the delineation of the main flowing features and showed that such features are directly or indirectly linked to karst phenomena. Understanding this complex flow system is critical for an appropriate assessment of groundwater resources and the design of sustainable groundwater production schemes.

Résumé La conduite d'une étude détaillée et exhaustive comprenant des volets géologiques, hydrauliques, géophysiques et géochimiques et portant sur les écoulements souterrains à proximité d'un forage dans un calcaire fracturé et karstifié démontre les potentialités d'une telle approche, dans les buts de localiser et caractériser les directions préférentielles des écoulements souterrains et les flux dans l'ouvrage au repos. La présente étude, menée à proximité d'un forage expérimental de 100 m sur l'île de Majorque, accomplit cette caractérisation à des échelles millimétriques à décamétriques. Les interprétations de pompages d'essai en trou ouvert et avec obturateur simple complètent en effet les résultats issus des diagraphies de production, des diagraphies de flux, de l'imagerie de paroi, des études de carottes et d'une analyse novatrice des fractures. Cette approche permet de dégager les caractéristiques des venues d'eau majeures et a montré que ces dernières sont directement ou indirectement liées aux phénomènes karstiques. La compréhension de ce système d'écoulement complexe est primordiale pour estimer adéquatement les ressources en eaux souterraines, et pour élaborer des plans durables d'exploitation de ces eaux souterraines.

M. Herfort · S. Loew
Engineering Geology Group,
ETH Zürich, 8093,
Zurich, Switzerland

N. Van Meir (✉)
Institut de Radioprotection et Sûreté Nucléaire,
IRSN/DEI/SARG/LETS, BP17, 92262,
Fontenay-aux-Roses, France
e-mail: nathalie.van-meir@irsn.fr
Tel.: +33-158359039
Fax: +33-146576258

P. A. Pezard · G. Lods
Laboratoire de Tectonophysique,
CNRS, Université Montpellier II,
Place Eugène Bataillon, CC049-34095,
Montpellier cedex 05, France

D. Jaeggi
Pfirter, Nyfeler & Partner AG,
Muttenz 4132, Switzerland

Resumen Un estudio geológico-hidráulico-geofísico-geoquímico de agua subterránea detallado e integrado del flujo de agua subterránea a los alrededores de un pozo perforado en caliza kárstica y fracturada muestra el poder de tal enfoque integrado para la localización y caracterización de rutas preferenciales de flujo de agua subterránea y flujo ambiental del pozo. El estudio, llevado a cabo en la proximidad de un pozo de investigación de 100 metros de profundidad en la isla de Mallorca, logra esta caracterización en una escala de milímetros a decenas de metros. Más específicamente el estudio añade interpretaciones de datos de preubas de packer sencillo y de bombeo de pozo abierto obtenidos durante mapeo fluido, medidas de flujo métrico con impeller, imágenes del pozo, descripciones del núcleos de barrenación y un análisis de fracturas innovador. Este enfoque permite la delineación de los rasgos principales del flujo y mostró que tales rasgos están directamente o indirectamente relacionados a fenómenos de karst. Entender el sistema de flujo complejo es crítico para una evaluación apropiada de los recursos de agua subterránea y para el diseño de esquemas de producción de agua subterránea sostenibles.

Introduction and objectives

Groundwater from fractured and karstified limestone forms a major component of the drinking water supply in many Mediterranean countries (Arfib et al. 2000; Custodio et al. 1991; Milnes and Renard 2004; Petalas and Diamantis 1999; Tulipano and Fidelibus 1996). Besides contamination and overdrafting, saltwater intrusion represents an additional hazard to such resources in coastal areas. The design and operation of sustainable groundwater withdrawal schemes in these hydrogeological settings require a rigorous understanding of the hydrogeological system, including type and properties of preferential pathways for groundwater flow. Several in-situ investigation methods for fractured/karstified limestone have been discussed in literature covering all kinds of technologies ranging from single and cross-hole transient pressure well testing (Karasaki 1990; Paillet 1993) to borehole geophysical and fluid logging (Hearst et al. 2000; Tsang and Hufschmied 1988; Tsang et al. 1990) and isotope geochemistry (Aeschbach-Hertig et al. 1998; Hoehn et al. 1998; Zanini et al. 2000) to surface geophysics (Parra et al. 2002; Skinner and Heinson 2004). An approach is presented here that aims at integrating geological, geochemical and geophysical properties measured under in-situ conditions at the borehole scale.

The present study was initiated in the context of the ALIANCE (Advance Logging Investigations of Aquifers in Coastal Environments) EC project (2002–2005), within a larger framework of saltwater intrusion problems in the northeast of the main Balearic island, Mallorca (Fig. 1). With support of the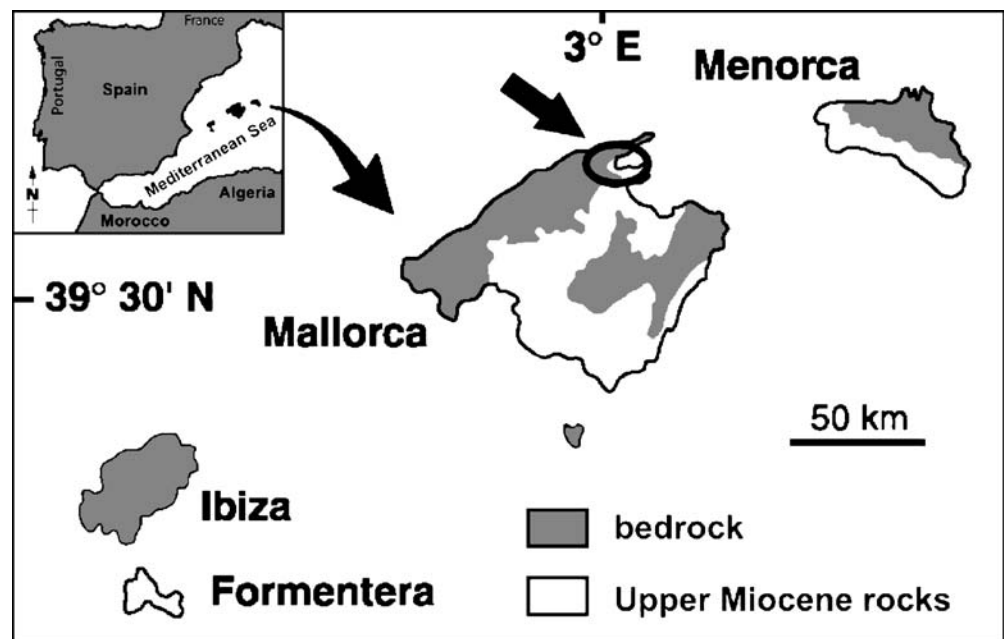 local Water Authority, a research borehole (called MP1) was drilled near the town of Pollença in the regional Lias aquifer, which consists of fractured and locally karstified limestone. To determine undisturbed hydraulic heads and to gather undisturbed depth-specific groundwater samples, testing was mainly carried out during drilling. The drilling fluid was traced and formation water samples were taken at several depths in conjunction with short single-well pumping tests. During a midway and a final logging campaign, borehole fluid flow and fluid composition were measured with various downhole logging tools (temperature, pH, oxygen, electrical conductivity, impeller flowmeter). Borehole and formation geometry and petrophysical properties were also measured with optical and acoustic borehole televiewers and a formation resistivity probe.
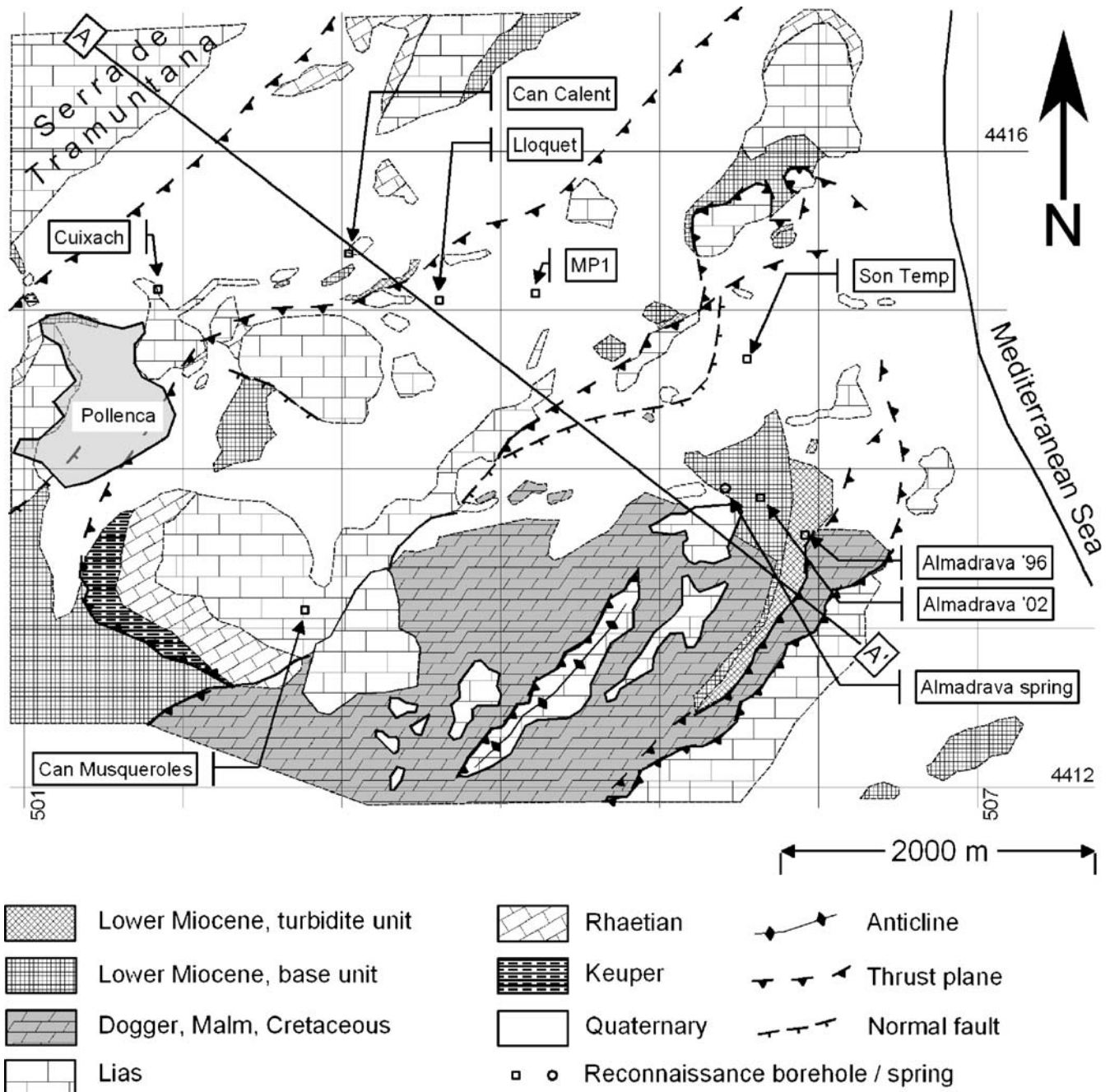
The geological and hydrogeological setting, the testing protocol and methods, and data analysis are described, and the value and detection limits of the different methods are compared. An integration of geological, hydraulic, petrophysical and fluid geochemical properties was carried out, leading to a rigorous understanding of the hydrodynamic system in the vicinity of the research borehole.

Regional geology and hydrogeology

The MP1 borehole, located in the northeastern part of Mallorca, lies in the Pollença plain at the foot of the Tramuntana mountain range (Serra de Tramuntana). Here, Alpine tectonics lead to a highly segmented geology with SW–NE aligned slabs (Figs. 2 and 3). A structural study of the region (Gelabert 1997) highlights its complexity with folds, faults and thrust sheets. The geological units playing a role in this study are the argillaceous sediments of Keuper age, the Rhaetian dolomitic marls, fractured and karstified Lias limestone and Miocene calcarenites and

Fig. 1 Map locating Mallorca and other Balearic Islands. The study site is in the northeast of Mallorca
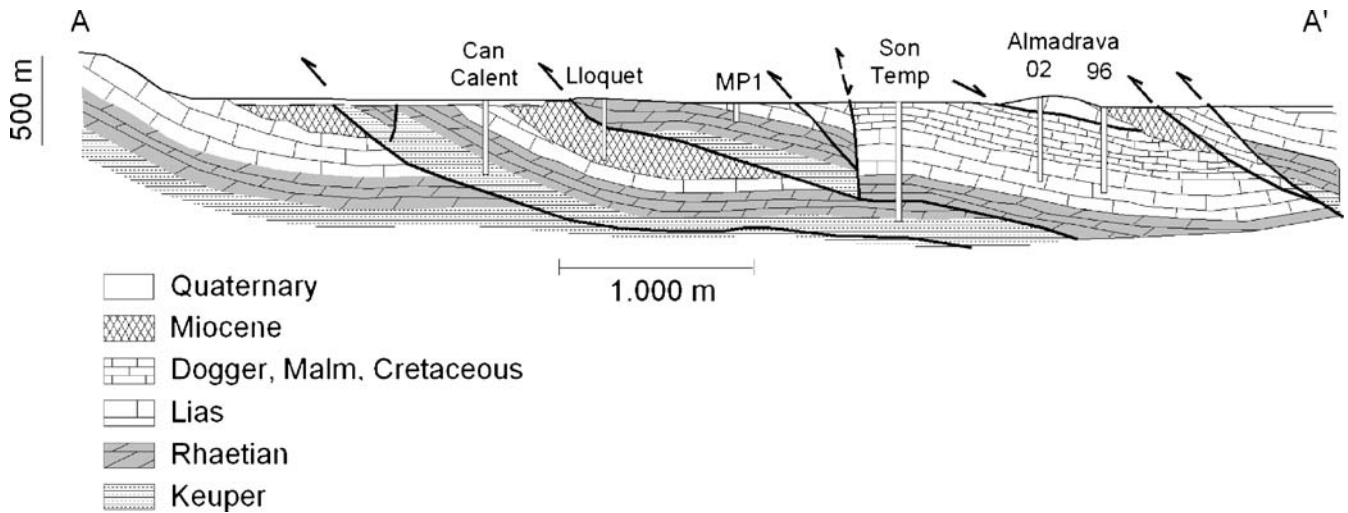
Fig. 2 Geological map of the northeastern part of Mallorca, after López García ([1999](#)), shows the location of boreholes *MP1* and piezometers *Can Calent* and *Can Lloquet*. Borehole 15 lies 1.5 km south off the map

turbidites. The Keuper sediments, acting as the main decollement plane, were partially pushed to higher levels along faults and form an impermeable boundary between different tectonic slabs (lamina).

The Lias limestone is heavily fractured due to Alpine tectonics. Local karstification enhances the hydraulic conductivity even more. This is documented by the Almadrava karst spring, where substantial amounts of groundwater from the Liassic aquifer discharge at the ground surface (Sanz et al. [2002](#)). The Almadrava Spring lies about 2 km away from the MP1 research borehole

(Fig. [2](#)). Hydrogeologically, the MP1 research drilling lies in an area where the main aquifer consists of Lias limestone. The aquifer can be either confined or unconfined. At the MP1 drilling the aquifer is unconfined. An average recharge of 230 mm/year comes from rainwater infiltration, return from irrigation and groundwater flow (González Casasnovas et al. [2000](#)).

Although the Balearic Water Authority has drilled a number of deep reconnaissance boreholes in this region over the last couple of years, very little piezometric data is available for longer periods in this part of Mallorca. In

Fig. 3 Geological cross-section along A-A' on Fig. 2, modified from López García (1999)

most of these recent boreholes only one large monitoring interval has been installed in the Lias-Rhaetian aquifer and this may cause hydraulic short-circuiting. Scarce piezometrical information shows a decreasing trend from 35 m amsl (metres above mean sea level) in 1974, to less than 20 m amsl in 2000 in the southern part of the unit (borehole number 15). Groundwater quality also deteriorated from values less than 100 mg/l TDS in 1983 to about 1,400 mg/l TDS today. Total dissolved solid content indicates a sea-water origin, although there is no direct contact with the sea (Barón Périz and González Casasnovas 1987; González Casasnovas et al. 2000). A field campaign carried out in the spring of 2002 confirms this hypothesis. Fluid electrical conductivity logs measured in these deep reconnaissance boreholes show a freshwater layer of variable (5–100 m) thickness above brackish water with a salinity of about 7,000 µS/cm (Fig. 4).
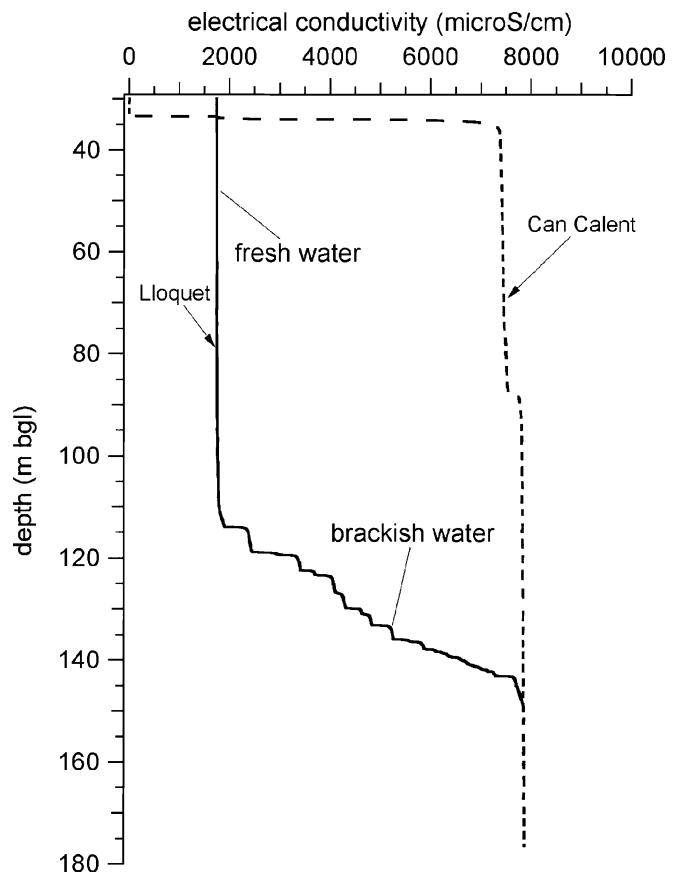
Some studies have tried to understand groundwater flow patterns in this region segmented by thrusts and overthrusts (Barón Périz and González Casasnovas 1987; Cardoso da Silva Junior 1997). Despite the quite large-scale isotope study by Cardoso da Silva Junior (1997), very little is known on how the different tectonic units are hydraulically linked. Gelabert et al. (1996) postulate that the individual thrust sheets are hydraulically separated domains that only communicate with each other at high water levels.

Site geology

The MP1 research borehole was drilled with a constant drill bit size of 104 mm diameter, using the wireline method. A PVC standpipe is installed from ground surface to 15.0 m depth. An extended litholog (Fig. 5) lists the most important geological features seen in the hole; a more detailed description follows.
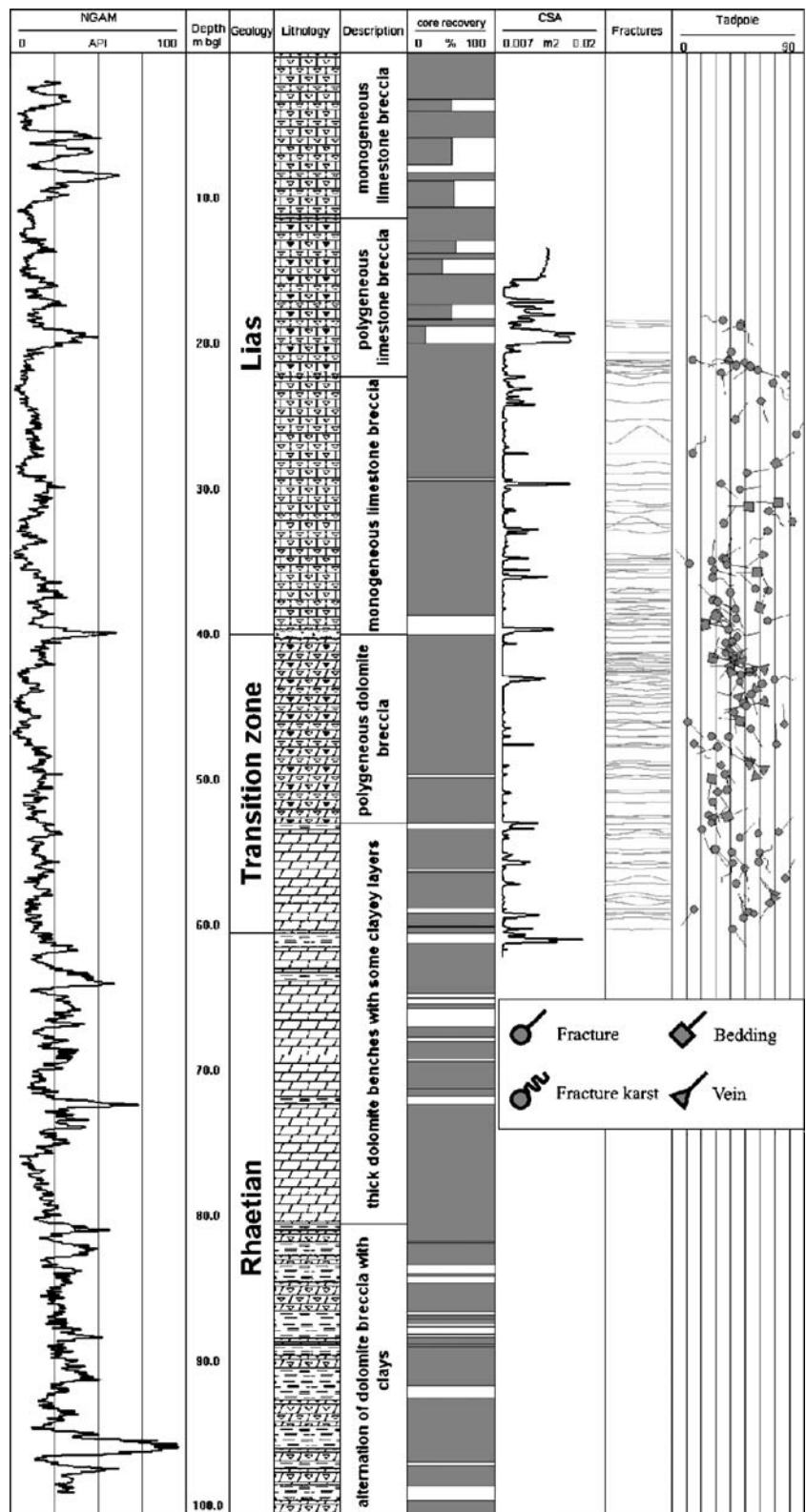
From top to bottom, the borehole first encounters fractured limestone of lower Lias age in which synsedimentary breccias are common. Cavernous weathering is typical due to the brecciated character of the rock. Down

to a depth of 11.4 m, a monogeneous limestone breccia is present. At 6.0 and 7.0 m depth, and especially between 8.0 and 10.0 m depth, large clay-filled karstic cavities are abundant. This sequence is followed by a polygeneous limestone breccia down to a depth of 22.3 m. Again, cavernous weathering is common and at 14.6 m a hardground horizon is present. From 18.5–20.0 m, large

Fig. 4 Example of electrical conductivity logs in the northeastern part of Mallorca, piezometzers *Lloquet* and *Can Calent* (location see Fig. 2)

Fig. 5 Geological description of the borehole with natural gamma (NGAM), core recovery percentage, cross-sectional area (CSA), fractures and fracture interpretation. *Tadpole tails* indicate the orientation (azimuth), and its position relative to a horizontal plane is defined by the dip angle between 0 and 90°

cavities occur again, partly filled with residual red-brown clays. Most of the core loss occurred within the first 20.0 m of the borehole, where karstic cavities complicated the drilling process.

From 22.3–39.7 m, a monogeneous limestone breccia reoccurs. At some depths, the rock looses its brecciated character. Cavities are still abundant at 24.0 and 34.0 m, but not to the same extent as before. At the bottom of this

section, from 39.7–40.3 m, a fault with relative displacements leading to the generation of a fault gouge is encountered. This gouge consists of coarse grained, partly rounded components of different colours floating in a fine grained clayey matrix with no cohesion. Within the matrix, a certain cleavage could be detected. The fault gouge is clearly identified by higher natural gamma radioactivity (Fig. 5) and by 100% core loss. Interestingly, within the adjacent rock fracture, density is not enhanced.

From 40.3–53 m, a polygeneous dolomite breccia is present. The rock is coarsely crystallised and calcite veins are common. From 40.3–60.6 m, the sediments have characteristics of both Lias and Rhaetian and are, therefore, defined as a gradual transition zone. Whereas bedding is not detectable within the massive Lias limestone, bedding is identified easily from core and borehole wall images below 50.0 m.

Below 53.0 m, thick dolomite benches interrupted by thin clays or clayey siltstones follow. The thick dolomite benches (up to 9 m thickness) consist of marly dolomites with a black lamination and dolomite breccias. From about 60.0 m onward, the natural gamma values (Fig. 5) are significantly higher than higher up, as a consequence of the more marly character of the beds; therefore, the top of Rhaetian has been set there (60.0 m). Cavernous weathering is present at 56.0, 75.0 and 78.0 m and highlights alteration from water circulation within the brecciated parts of the rock. The clayey siltstones are not thicker than 1 m and sand- to gravel-sized partly rounded dolomite components are usually floating within the colourful clayey matrix. The components seem to originate from the adjacent host rock. In most cases, formation as a consequence of tectonic displacements does not seem plausible due to the lack of structural indications. The Rhaetian unit extends down to 80.6 m.

Below 80.6 m, alternating beds of reddish monogeneous dolomite breccia with clays are obtained. The thickness of these separate beds does not exceed 2 m. Fractures within the dolomite beds are mostly filled with clay from the adjacent beds. The 100-m-deep borehole did not reach the Keuper formation, which is supposed to act as the main impermeable boundary in the region, nor did it reach the main thrust plane proposed by López García (1999).

Depth accuracy of the lithological log is an important issue, especially for the fracture analysis described below. The depth recorded during drilling is not very precise and a reference log for true depth, usually the natural gamma log, is required. Discrepancies between gamma depth and driller's depth are strongly dependent on the local core loss and therefore drilling technique and rock quality. Between 0 and 20 m, where extensive core losses occurred, depth discrepancies are theoretically possible up to the full length of the core barrel, which was 3 m. After a comparison of the cores with the optical televiewer images, the depth discrepancy in this interval is limited to 2 m. In the vicinity of moderate core losses observed at 39, 66, 84, 92 and 99 m depth, shifts can reach up to 1 m. For the rest of the borehole, observed discrepancies are

smaller than 40 cm. If one looks at the cross-sectional area (CSA) log and compares it to the recovery representation in Fig. 5, it becomes clear that borehole enlargements occur mostly in zones of core loss. These zones are either
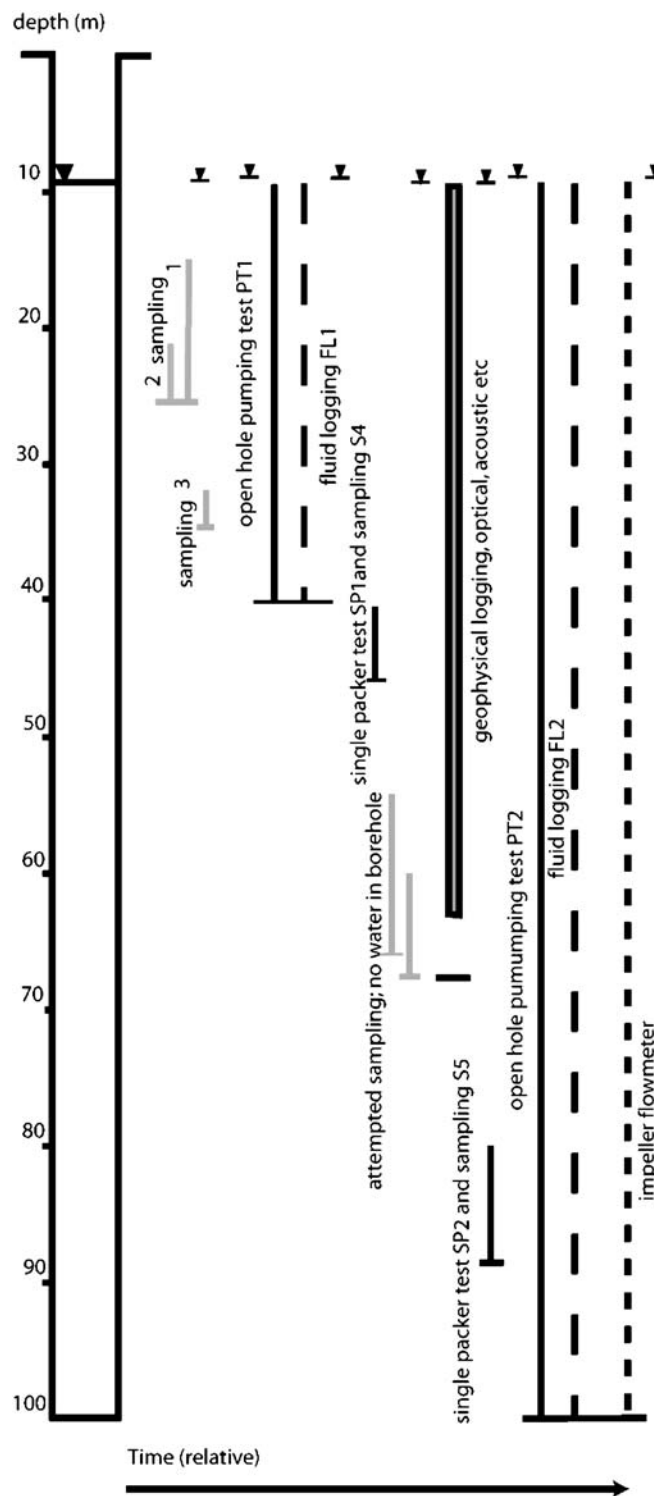

Fig. 6 Borehole with a relative time axis indicating all sampling, logging and testing along with water depth measured at different stages. *Markers in grey* signify the sampling of the water table on five occasions

Table 1 Summary of the results from hydraulic testing

Experiment and date	SP 105.09.2002	SP 223.09.2002	PT 130.07.2002	PT 230.09.2002
Tested interval (m bgs) interval length	41.1–46.5 (5.4 m)	80.3–88.2 (7.9 m)	9–33 (24 m)	9–101 (92 m)
Aquifer unit (thickness)	Lias (~40 m)	Rhaet (~132 m)	Lias (~40 m)	Lias + Rhaet (~172 m)
Pumping rate (l/s)	0.25	0.15	0.31	1.2
Duration	4 h 8 min 54 s	4 h 54 min	2 h 7 min 31 s	5 h 50 min
Transmissivity (m^2/s)	6.9E-4	1.3E-5	4.7E-4	1.6E-3
Hydraulic conductivity (m/s)	1.3E-4	1.6E-6	2.0E-5	1.7E-5

SP single-packer test, *PT* pumping test, *bgs* below ground surface

strongly karstified (e.g. at 18 and 20 m depth) or consist of marly material (e.g. at 40, 53.3 and 61 m depth).

Methodology and testing protocol

The testing protocol and methods are presented here to give a relative time- and depth-dependent overview of the investigations carried out. As mentioned before, borehole MP1 was a pilot borehole drilled to see how well the site was suited for the ALIANCE project objectives and to get a better insight on the formation and groundwater characteristics before setting up a larger test site. In order to speed up this decision process, much of the testing started at the same time as the drilling (Fig. 6). The testing was carried out over three main intervals, at 40, 60 and 100 m depth.
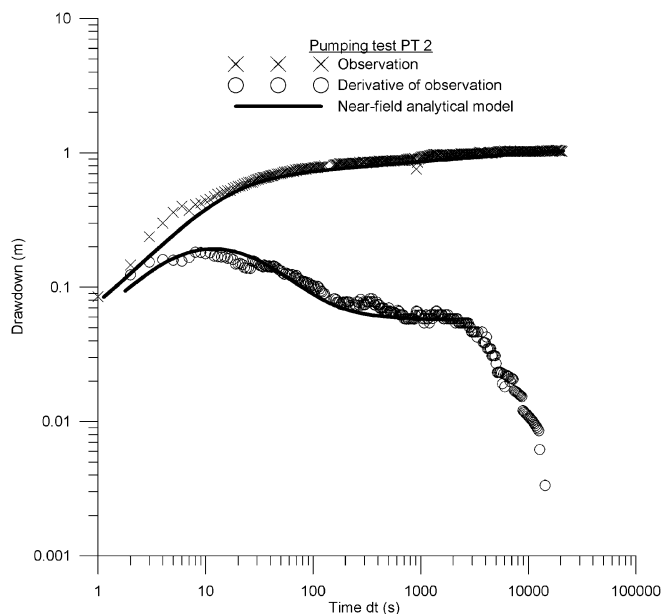
Hydraulic testing consisted of single packer tests performed at different depths, and open-hole pumping tests at two stages of borehole development (40 and 100 m depth). Over the same two intervals, fluid-logging experiments added information on transmissivity and indicated major and minor inflow zones. Impeller flowmeter logging complemented the hydraulic testing and inflow zone characterisation. Optical and acoustic borehole wall images were obtained when the borehole reached 62 m depth. The acoustic televiewer measurements of the two-way travel time also indicated borehole size and cross-sectional area. Optical borehole televiewer pictures, along with acoustic images available from 16–60 m, were used to identify and map planar features observed in the hole such as fractures, bedding planes and veins (Figs. 5 and 15), in addition to evaluating the discontinuities of the rock with measurements on core material. From the recorded two-way travel time, the borehole diameter and cross-sectional area are calculated (Fig. 5).

The core was systematically described for lithology and fracture characteristics. Groundwater samples were also taken at several depths. As drilling fluid came from a nearby well tapping the same aquifer, it was important to distinguish formation water from drilling fluid during sampling. To this end, the drilling fluid was traced with Sulphorhodamine B, and the pumped water monitored on-site with a field fluorimeter (GGUN-FL30; Schnegg and Doerfliger 1997). When the percentage of drilling fluid was less than 10%, a sample was taken and the composition back-calculated.

Data analysis

Single packer and open hole pumping tests

Single packer tests derive a transmissivity value for smaller sections of the borehole as drilling progresses, whereas pumping tests evaluate overall transmissivity of the borehole. In the MP1 borehole, two single packer (SP1 and SP2) and two pumping tests are interpreted (PT1 and PT2; Table 1, Fig. 6). SP1 and PT1 both only test the upper aquifer, the Lias. The second packer test studies part of the Rhaetian aquifer, and finally, the second pumping test (PT2) involves both Lias and Rhaetian sediments. As both single packer and pumping tests last for only short periods, a constant thickness as well as homogeneous behaviour for both Lias and Rhaetian aquifers is considered in the interpretation. Analytical models of transient radial flow towards the well were fitted to the observed drawdown (Fig. 7). This semi-quantitative approach was applied because the complex subsurface structure cannot be derived with confidence from the short-term, single-well pumping test data. The hydraulic conductivity (transmissivity divided by the length of the tested borehole interval) varies with depth. Generally, the value

Fig. 7 Log-log plot of drawdown vs. time for pumping test 2

for the Rhaetian is about two orders of magnitude smaller than the hydraulic conductivity of the Lias (Fig. 8). PT2, which tests both Lias and Rhaetian, gives an intermediate hydraulic conductivity, dominated by the upper, more conductive aquifer unit.

Fluid logging

A fluid-logging experiment allows the identification of permeable flow zones, and the computation of their transmissivities in a borehole when the aquifer is subjected to a known hydraulic stress, by recording transient changes of electrical conductivity and pressure in the fluid after flushing the borehole with a fluid of different conductivity (Tsang et al. 1990). Here, two experiments are interpreted. The first fluid-logging experiment started on 1 August 2002 when the borehole was 40.7 m deep; drilling had ended 2 h previously (Table 2).
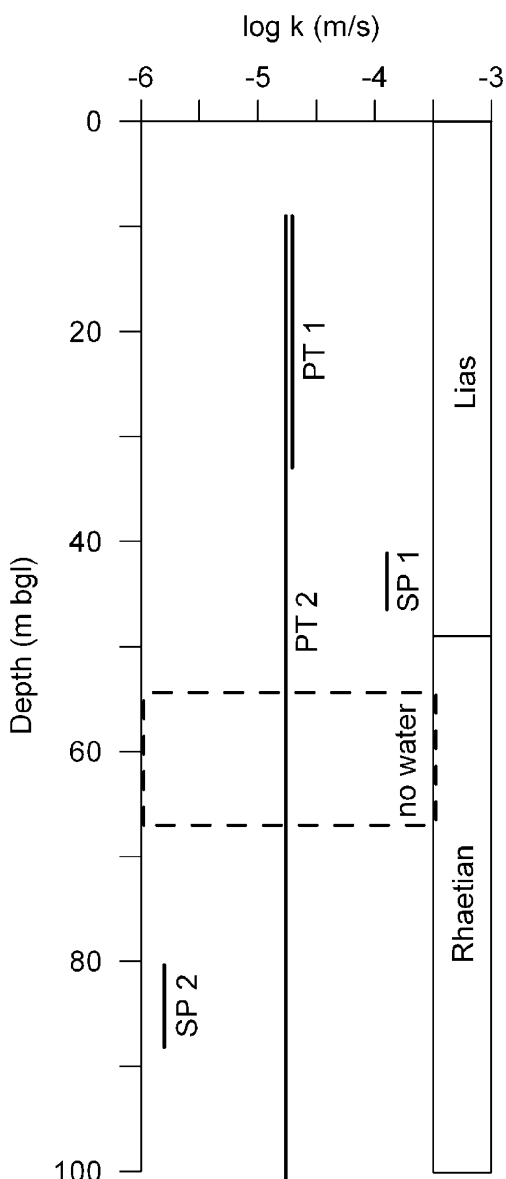
Fig. 8 Profile of hydraulic conductivity (for symbols see Table 1)

The second experiment started on 1 October 2002, after borehole completion at 100 m depth. The borehole had been completed 4 days earlier. Practical set-up details are listed in Table 2. Water in the MP1 borehole had an average electrical conductivity value of about 1,300 μS/cm. The flushing water, rainwater, had an average of 100 μS/cm, and was injected through the drilling stem. A first electrical conductivity profile measured the extent of the flushing and can give an indication of ambient flow in the borehole. After this log, pumping started and consecutive electrical conductivity profiles were recorded until pre-flushing conditions were reached.

For the interpretation of the change in electrical conductivity with time, a one-dimensional advection-dispersion numerical model called "BORE" (Hale and Tsang 1988) that calculates fluid concentration changes from given inflow rates and inflow concentrations for different inflow points was used. There are four unknown parameters, inflow rate, inflow location, inflow concentration, and time of inflow start. These four unknowns were changed through trial and error until a good match was found between calculated concentration profiles at different times and observed concentration profiles at the same times.

Spatially, the borehole is divided into cylindrical elements with a constant height of 0.25 m. The cross-sectional area and volume, needed for the transport simulation, are then calculated with a borehole diameter of 104 mm. Time steps for the advection-dispersion calculation last 0.05 min. As the numerical model simulates changes in concentration, the recorded electrical conductivity (σ) is converted to concentration of TDS (total dissolved solids) with the following empirical equation (Tsang and Hufschmied 1988) :

$$\sigma(\mu S/cm) = 1850 \times C(kg/m^3) \tag{1}$$

According to Tsang and Hufschmied (1988), this equation is valid for low-salinity water up to an electrical conductivity of 8,000 μS/cm. After the model simulation, the calculated concentrations are reconverted to electrical conductivity, making it easier to display the output and observed conductivity profiles together.

When pumping starts, the consecutive electrical conductivity logs show how the flushing fluid and formation water re-enter the borehole through permeable features. The fitting procedure starts after steady state has been reached (from the third log, after 18 min of pumping for the first test). The initial concentrations are derived from the steady state concentration profile (Fig. 9). The lower boundary of the borehole is assumed to be a no-flow boundary; the upper boundary is the discharge boundary. Dispersion is considered constant and equal to 5.10^{-4} m^2/s. To fit the observed conductivity changes in the first experiment, a total of 14 inflow points are defined (Table 3). Each point has a depth, inflow TDS concentration, inflow rate, and a time at which inflow starts. The best fit is shown in Fig. 9 and results are

Table 2 Technical details for both fluid-logging experiments

Experiment	Discharge rate	Flushing volume	Flushing fluid conductivity	Number of logs	Total testing time	Average drawdown
40 m deep	3 l/min	750 l	108 μS/cm	11	2.5 h	6 cm
100 m deep	7 l/min	1,200 l	178 μS/cm	5	2 h	4.5 cm

summarised in Table 4. The sum of the modelled inflow rates is 2.82 l/min, which is close to the pumped discharge rate of 3 l/min.
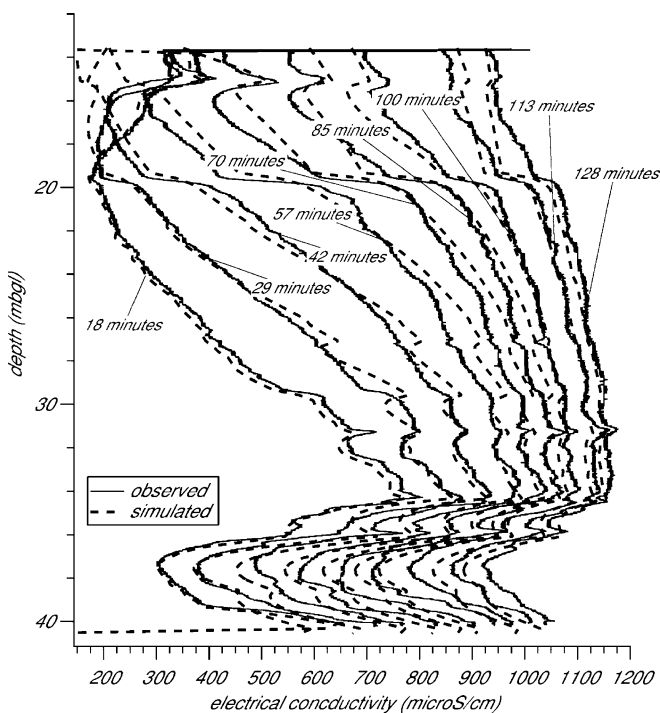
The most important inflow points are located, in order of importance, at 15.0, 19.45, 34.20, 35.97, 27.15, and 29.54 m depth. Fitting the slowly rising slope between 20.0 and 30.0 m required three smaller inflow points to be inserted. The relative unimportance of these inflow points is reflected when the inflow rates are represented as a percentage of the total pumped discharge rate (Table 4).

Because the inflow water concentration in the model is constant, it is necessarily an average value between a lower concentration in the beginning of the inflow, and a higher concentration at later stages of the test. This is particularly important in the upper part for the inflow points at 15.0 and 19.45 m depth. In the logs between 18 and 42 min after pumping starts, the concentration at 15.0 m is constant and even slightly lowers; at 19.45 m a concentration step develops progressively during the test, indicating that concentration differences increase at least up to 57 min after starting the pump. This supports the hypothesis that the flushing fluid has primarily entered this feature and is releasing low-salinity (flushing fluid) water. Just below 19.45 m, the concentration was higher from the

start of the test and moves up slowly, increasing the step in concentration at 19.45 m. The flushing fluid, leaving the 19.45 m feature, is then drawn towards the pump and keeps the concentration at 15.0 m lower than expected. For these reasons, and in order to achieve a good fit between measured and calculated concentration changes, inflow at 15.0 and 19.45 m starts only about 1 h after start of pumping. These two features also have the highest inflow rate. The volume flowing out of these features in this time is about 50 l.

In the second experiment, steady state for drawdown is reached after 39 min (Fig. 10). This profile is used as a starting point for the analysis. The electrical conductivity profile after 153 min is close to the original conductivity profile before flushing, and the analysis stops there. Discharge rate in these five logs is constant and is equal to 7 l/min. To obtain a good fit between observed and calculated electrical conductivity profiles, 13 inflow points are defined. Again, each inflow point has an inflow concentration, an inflow rate and a time when flowing from this feature starts (Table 5). Dispersion is constant and equal to 5.10^{-4} m^2/s. The most important inflow point is at 55.5 m, followed by the inflows at 47.2, 74.8 and 20.0 m depth.

The second experiment shows fewer, but more important inflow features, and it confirms the large inflow point at 20.0 m depth (Fig. 10). To fit this point, the inflow starting time is delayed by about 1 h, giving a volume of 64.8 l for this feature. The same concentration step (or crossing of the curves at 39 and 73 min) at this depth was observed as in the first experiment, indicating that water flowing out of this feature has a lower concentration than water below this feature. There is no fit for the feature at 15.0 m, because recordings stop at this depth. Again, as in

Fig. 9 Fluid-logging fit to experiment 1. It represents the consecutive electrical conductivity profiles after flushing and reaching steady state after 18 min

Table 3 Model input for fluid-logging experiment 1

Depth (m)	Inflow rate (m^3/s)	TDS Conc. (kg/m^3)	Flow start time (h)
15.00	8.00E-6	0.55	0.8
19.45	7.00E-6	0.3	1.1
21.50	1.00E-6	0.5	0
24.00	1.00E-6	0.5	0
26.00	1.00E-6	0.6	0
27.15	5.00E-6	0.6	0
29.54	5.00E-6	0.65	0
31.42	3.00E-6	0.70	0
32.00	1.00E-6	0.70	0
33.00	1.00E-6	0.70	0
34.30	0.60E-5	0.74	0
35.97	5.00E-6	0.74	0
38.52	1.00E-6	0.74	0
40.22	2.00E-6	0.74	0

Table 4 Transmissivity (T) results for both fluid-logging experiments and the associated inflow rates (Q)

Depth (m)	Q (l/min)	% inflow	T (m^2/s)
Fluid-logging experiment 1			
15.00	0.48	17.02[a]	$1.42 \cdot 10^{-4}$
19.45	0.42	14.89[a]	$1.24 \cdot 10^{-4}$
21.50	0.06	2.13	$1.78 \cdot 10^{-5}$
24.00	0.06	2.13	$1.78 \cdot 10^{-5}$
26.00	0.06	2.13	$1.78 \cdot 10^{-5}$
27.15	0.3	10.64[a]	$8.86 \cdot 10^{-5}$
29.54	0.3	10.64[a]	$8.86 \cdot 10^{-5}$
31.42	0.18	6.38	$5.31 \cdot 10^{-5}$
32.00	0.06	2.13	$1.78 \cdot 10^{-5}$
33.00	0.06	2.13	$1.78 \cdot 10^{-5}$
34.30	0.36	12.77[a]	$1.06 \cdot 10^{-4}$
35.97	0.3	10.64[a]	$8.86 \cdot 10^{-5}$
38.52	0.06	2.13	$1.78 \cdot 10^{-5}$
40.22	0.12	4.26	$3.55 \cdot 10^{-5}$
Total	2.82	100	$8.33 \cdot 10^{-4}$
Fluid-logging experiment 2			
20.00	0.9	13.04[a]	$3.37 \cdot 10^{-4}$
21.50	0.102	1.48	$3.83 \cdot 10^{-5}$
24.28	0.102	1.48	$3.83 \cdot 10^{-5}$
34.00	0.3	4.35	$1.13 \cdot 10^{-4}$
47.20	1.44	20.87[a]	$5.4 \cdot 10^{-2}$
48.60	0.024	0.35	$9 \cdot 10^{-6}$
55.50	1.8	26.09[a]	$6.76 \cdot 10^{-4}$
61.00	0.24	3.48	$9 \cdot 10^{-5}$
64.00	0.6	8.70	$2.25 \cdot 10^{-4}$
66.00	0.06	0.87	$2.25 \cdot 10^{-5}$
74.80	1.2	17.39[a]	$4.5 \cdot 10^{-4}$
84.20	0.042	0.61	$1.58 \cdot 10^{-5}$
94.00	0.09	1.30	$3.37 \cdot 10^{-5}$
Total	6.9	100	$2.59 \cdot 10{-3}$

[a] Indicates main inflow points

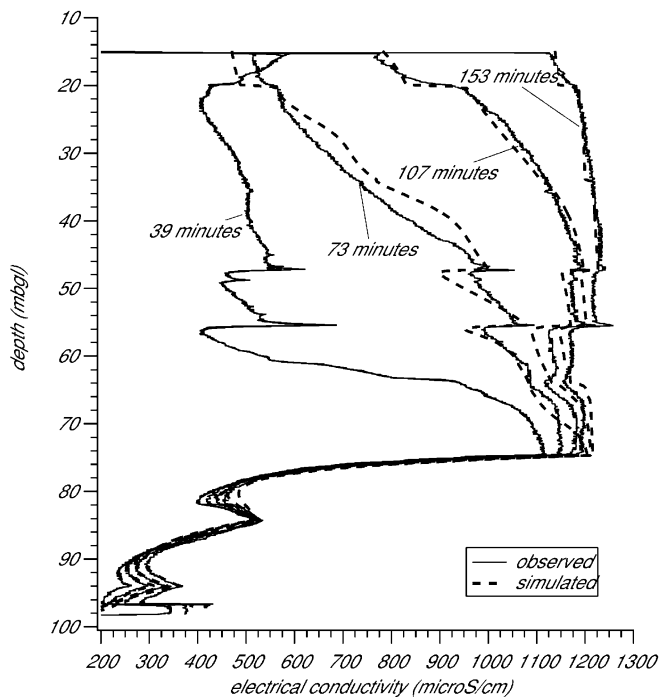**Fig. 10** Fluid-logging fit to experiment 2. It represents the consecutive electrical conductivity profiles after flushing and reaching steady state after 39 min

the first experiment, two smaller inflow points between 20.0 and 30.0 m are inserted to reproduce the increasing slope at this depth. The sum of inflow rates is 6.9 l/min.

A rough estimate of total transmissivity is derived from the ratio between discharge rate and steady state drawdown. Only the transmissivities can be compared directly between the two experiments. The second experiment includes the range of the first experiment, but does not reflect all features recognised in the first experiment. This is probably due to the fact that the larger feature in the second experiment overprints some features. However, the most important features obtained in the upper 40.0 m, are also detected in the second experiment (20.0 and 34.0 m) and they are fitted with comparable transmissivities.

Ambient flow

Identifying ambient flow, or the flow within a borehole as a consequence of short-circuiting different geological layers with different potentials, is important for a number of reasons. The first reason is to stop hydraulic short-circuiting that may cause a change in the groundwater quality profile. The second is that it may give an indication of regional flow patterns. Finally, it is important to know ambient flow patterns in the borehole to correct the conducted tests. In this case, information on ambient flow is obtained after flushing the borehole with rainwater,

before pumping, and from water level measurements during drilling. These measurements were taken every morning after an average of 16 h of rest (Fig. 6).
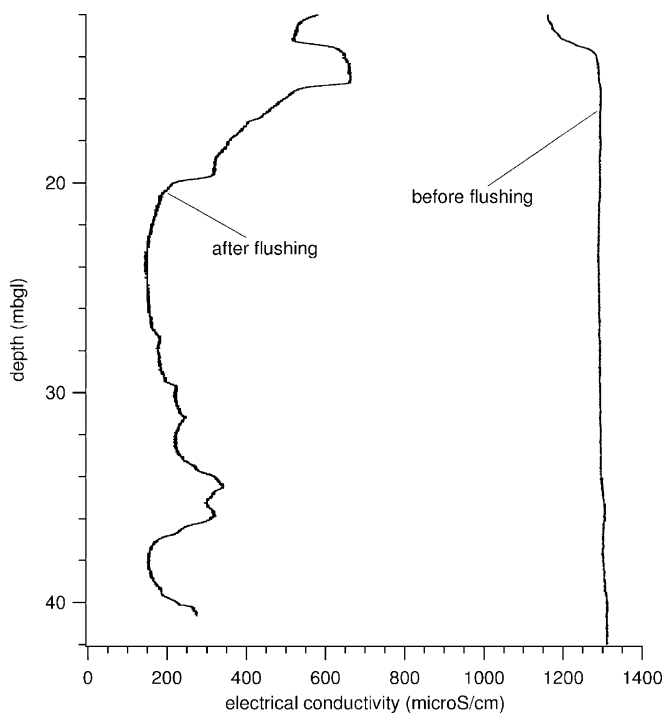
In both fluid-logging tests, the borehole has a quasi-constant water electrical conductivity of 1,275 µS/cm, slightly increasing above 1,300 µS/cm towards a depth of 40.0 m, before the fluid-logging experiment. In the first experiment, the flushing fluid (rainwater) with an electrical conductivity of 108 µS/cm is injected at the bottom of the borehole at 40 m depth through the drilling stem. The flushing fluid flows upward because of the applied pressure, and pushes the higher electrical conductivity water into the formation. This situation is reflected in the first electrical conductivity profile, measured after the drilling stem was removed from the borehole and before pumping (Fig. 11). None of the flushing fluid reached the
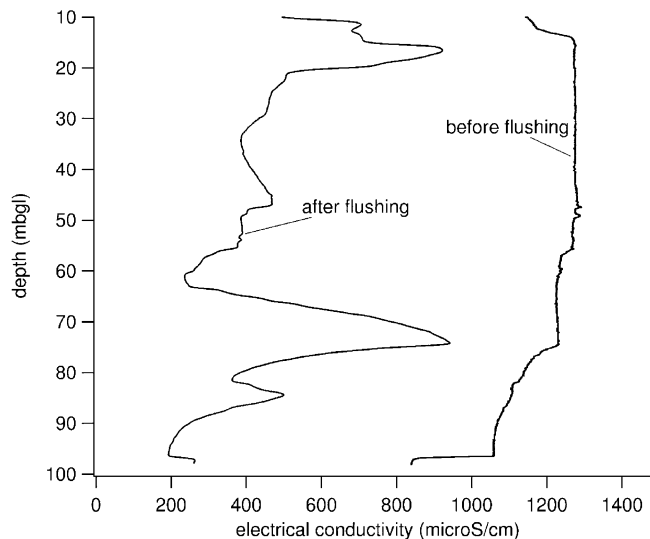
Table 5 Model input to fluid-logging experiment 2

Depth (m)	Inflow rate (m^3/s)	TDS Conc. (kg/m^3)	Flow start time (h)
20.00	1.50E-5	0.50	1.2
21.50	1.70E-6	0.50	0
24.28	1.70E-6	0.50	0
34.00	0.50E-5	0.50	0
47.20	2.40E-5	0.73	0
48.60	4.00E-7	0.60	0
55.50	3.00E-5	0.70	0
61.00	4.00E-6	0.60	0
64.00	1.00E-5	0.60	0
66.00	1.00E-6	0.60	0
74.80	2.00E-5	0.72	0
84.20	0.70E-6	0.60	0
94.00	1.50E-6	0.35	0

surface, indicating that all of the fluid entered the formation. The interval located between 20.0 and 32.0 m has the lowest hydraulic conductivity (Fig. 8). Between 37.0 and 39.0 m depth, the electrical conductivity is also low and close to the flushing fluid conductivity, between 34.0 and 37.0 m depth electrical conductivity is slightly higher, and above 20.0 m, electrical conductivity is much higher, increasing towards 15.0 m. The differences in electrical conductivity, after flushing, are explained by several mechanisms: ambient flow, a lower permeability or variations in borehole diameter. The higher electrical conductivity at the depth between 34.0 and 37.0 m can be explained by ambient flow, as these features are not characterised by a higher natural gamma signal, a change in geology or a change in borehole diameter. Smaller features at 27.0 and 29.0 m may also be a consequence of outflow at a permeable feature. Although the evidence is small, it is later confirmed by the interpretation of the entire fluid-logging event, where these depths coincide with important flowing features. Near 20.0 m depth, there is no direct evidence of ambient flow, but, where most of the flushing fluid enters, it may be a point of high permeability or low potential. This would explain the higher electrical conductivity above 20.0 m, as there was less fluid to flush the upper part of the borehole between 20.0 and 15.0 m.

In the second fluid-logging experiment, the evidence of ambient flow is much clearer (Fig. 12). A high electrical conductivity peak present at 74.8 m depth coincides with a zone of strong cavernous weathering. In the electrical

Fig. 12 Flushing profile in fluid-logging experiment 2. It shows the influence of possible ambient flow at the depths of 47, 55 and 74.8 m

conductivity log taken before flushing, the conductivity decreases slightly at this depth as well. The peak reflects an upward flow indicating ambient flow. At the depth of 55.0 m, there is another step in the pre-flushing electrical conductivity log and a smaller peak in the flushed profile. Core analysis indicates a strongly fractured and fissured region so that, again, ambient flow is the most likely explanation. The same may be true at 47.0 m depth, but there is less evidence. Above the depth of 20.0 m, there is a strong increase in electrical conductivity in the flushed profile. Again, it is hypothesised that most of the flushing fluid entered at 20.0 m depth and left little fluid to clean the borehole above this depth.

In summary, there is evidence for ambient flow in both experiments, detected by the flushed electrical conductivity profile before pumping starts. The water level variations measured during drilling are small, but show a slight increase towards greater depth (Fig. 5).

Impeller flowmeter logging

The impeller flowmeter (IFM) testing also indicates discrete inflow points when run in a fractured media, and can result in transmissivity estimates for these inflow points. A standard procedure for impeller flowmeter testing is to run the tool up and down the borehole with different cable speeds without pumping water, followed by running the tool at the same speeds again while pumping. The logs without pumping measure ambient flow in the borehole and need to be subtracted from the logs run with pumping in order to identify the flow zones. For more information on standard impeller flowmeter testing see for example Hearst et al. (2000) and Paillet (1995). A laboratory or field experiment calibrates the tool for the conversion from the measured rounds per minute (RPM) to the desired velocity. By multiplying velocity

Fig. 11 Flushing profile in fluid-logging experiment 1. This figure gives a first impression of possible ambient flow at depths of 27, 29 and 34–37 m

with the cross-sectional area, velocity is converted into outflow rate.

Table 6 summarises the IFM experiment details. The recorded RPM are converted to velocity with a calibration curve set up in the stand pipe of the borehole, with a diameter of 130 mm. The inflow rates are then calculated by multiplying the velocity with the cross-sectional area, derived from the acoustic televiewer log. An important note concerns the recording between the depths of 15.0 and 20.0 m. Here, the acoustic televiewer recording is typical of a tool that is located off-centre in the hole, and receives dummy signals as the recording time window is exceeded. Therefore, only the values for the cross-sectional area between 20.0 and 60.0 m depth were used to calculate the inflow rate from velocity.
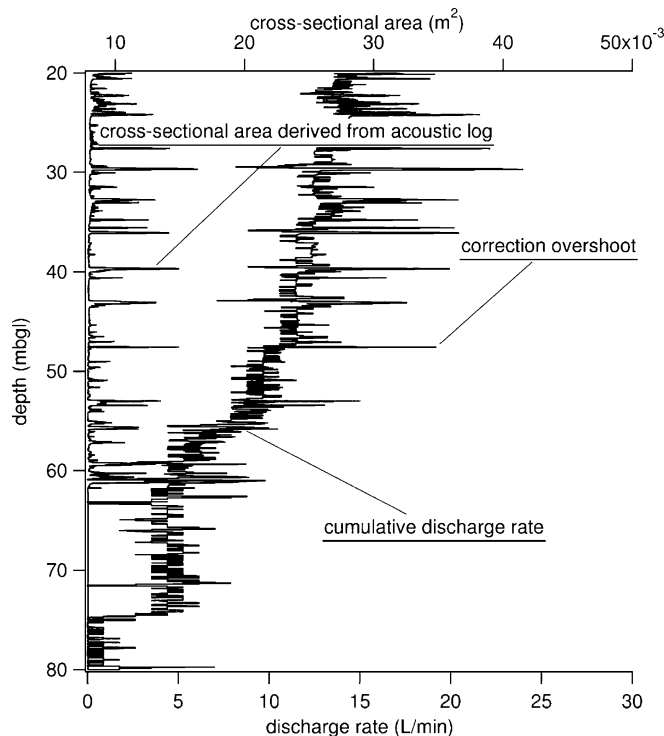
The difference between the recorded rounds per minute (RPM) for the ambient logs going up and down is close to zero. A maximum difference of 4 RPM is calculated, but this is within error-bar range ($\pm$7 RPM). In contrast to the fluid-logging experiment, the IFM does not detect any ambient flow, an indication that, in this particular setting, fluid logging is the more sensitive method. From the outflow rates (Fig. 13), one can differentiate four different inflow zones: one at 74.8 m depth, one inflow zone between 54.0 and 58.0 m depth, a third zone between 47.0 and 49.0 m and the fourth is a large zone where inflow slowly increases between 30.0 and 38.0 m. From the inflow axis, the inflow rates for each zone were obtained (Table 7). Assuming a total discharge rate of 14 l/min, the percentage for each feature compared to the total outflow rate was calculated. Although the analysis presented here is for a cable speed of 3 m/min, the same is true for the runs at 6 m/min. The logging at higher cable speed, however, is noisier. The IFM data display a smoother increase in total discharge rate compared to the fluid logging that identifies specific features. The same important features as derived from the fluid-logging experiment are noticed here (47.0, 56.0, 61.0 and 74.8 m depth), but the impeller flowmeter shows a slow increase, whereas the fluid-logging method indicates point inflow. In this case, the latter derives more detailed information.

Hydrochemistry

As drilling progressed, samples were taken at several intervals. In most cases, the sampled water was mixed with a percentage of drilling fluid. As the drilling fluid was traced with Sulphorhodamine B with a concentration of 200 µg/l (ppb), it was possible at any time to derive the
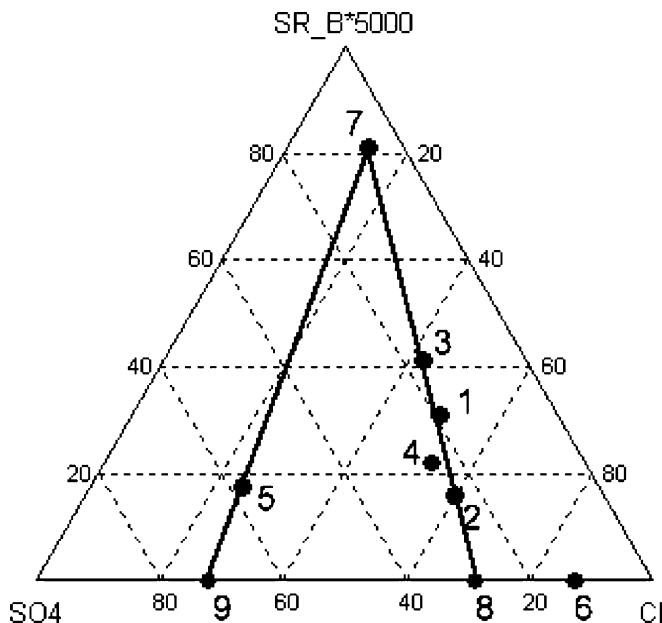

Fig. 13 Inflow rates from the impeller flow meter logging experiment and cross-sectional area derived from acoustic logging. The cumulative discharge rate is corrected for changes in borehole diameter

true water composition of the sample. A ternary diagram (Fig. 14) displays the relative percentage of sulphate, chloride and Sulphorhodamine B. The base line of this diagram defines the sulphate/chloride ratio and was chosen to separate Lias and Rhaetian groundwater, because the Rhaetian includes gypsum-bearing sediments. The Sulphorhodamine-B axis is stretched 5,000-fold in order to compensate for differences in concentration magnitude. All samples taken above 47 m bgl define a mixing line between the drilling fluid (7) and Lias type water (8). The latter represents a calculated composition and corresponds to the drilling fluid before the tracer was added. Water pumped for drilling fluid comes from a nearby water supply well that taps the uppermost part of the Lias aquifer. Sample 4 is influenced by the Rhaetian type water (9) and therefore plots to the left of the mixing

Table 6 Summary of impeller flowmeter runs

Cable speed	Direction	Ambient	Discharge rate (l/min)		Pump depth
3 m/min	Up and down	Done	10	20	11.5 m
6 m/min	Up and down	Done	10	20	11.5 m

Table 7 Transmissivity (T) results and percentage inflow calculated for the flowmeter logging experiment

Depth	Q (l/min)	%inflow	T (m^2/s)
24–25	1.00	7.14	$1.49.10^{-4}$
34.5–35	1.00	7.14	$1.49.10^{-4}$
40–42.5	1.00	7.14	$1.49.10^{-4}$
47.4–49	2.00	14.29	$2.97.10^{-4}$
56–59	4.00	28.57	$5.94.10^{-4}$
61–62	1.00	7.14	$1.49.10^{-4}$
74.8	4.00	28.57	$5.94.10^{-4}$
Total	14.00	100.00	$2.08.10^{-3}$

Fig. 14 Mixing of drilling fluid and groundwater for samples obtained during the drilling process. *SR_B* Sulphorhodamine B, 5000-fold exaggerated; *SO4* sulphate; *Cl* chloride; *1* MP1 23.50–25.0 m; *2* MP1, 16.00–25.0 m; *3* MP1, 32.50–35.2 m; *4* MP1, 41.10–46.6 m; *5* MP1, 80.30–88.2 m; *6* sea water, *7* drilling fluid, *8* Liassic water, *9* Rhaetian water. Percentage was calculated from mass concentration (i.e. mg/l) rather than from mol or equivalent concentrations

line. Sample 5 together with the drilling fluid (7) define the Rhaetian type water (9), which again is a calculated composition. Due to the huge amount of drilling fluid injected, the pure Rhaetian type water could not be sampled directly, even after hours of pumping. The groundwater composition distinguishes the Lias aquifer from the Rhaetian (Table 8). Tracing the drilling fluid was essential to extract the groundwater composition of the deeper aquifer unit (Rhaetian).

Discussion and fracture analysis

A number of flow zones have been identified from in-situ testing and data modelling. There is a high consistency in results between the fluid-logging experiment and the impeller flowmeter test, and they are ranked according to relative transmissivity. However, to connect these features to a geological explanation, the cores and borehole wall images need to be more closely investigated.

From the analysis on optical and acoustic high-resolution images as well as inspection of core materials, a total of 123 features are identified in MP1, among which 66 fractures, 16 veins and 9 bedding planes are determined with high confidence. Within the upper part of the borehole, from 16.0 to 20.0 m, a lot of cavities are present. Fractures are enlarged by dissolution, and consequently, measurements of orientation are not precise. From 34.0 to 36.0 m, and from 45.0 to 49.0 m, two zones with several wide fractures occur. Here, the orientation determination was easy and the fractures compare to those found on cores. The planar fracture surfaces are coated with thin red clay. The surrounding of these fractures is often strongly re-crystallised, which points to processes involving water flux through the fracture. At 53.0 to 60.0 m a section with a lot of borehole enlargements occurs, probably due to soft marly or clayey zones.

Even though the dataset with 123 measured features is quite small, the main characteristics of the structure can be determined from this set. Strikes of fractures and veins are parallel to the strike of tectonic structures which is SW–NE (Fig. 15). Only one family of fractures could be evaluated in which fractures dip 30° to SE, with a strike vertical to tectonic transport. More common fracture sets have non-homogeneous orientations. The main fracture set could be interpreted as tension cracks due to foldbending observed in this area. Veins could not be identified above 41.0 m. The bedding dataset is too small for a spatial analysis and uncertainty of orientation is high.

In general, the results derived from fluid logging, impeller flowmeter and pumping tests show Lias sediments to be more permeable than the Rhaetian (up to two orders of magnitude). The most important flow zones lie within the Lias and the transition to the Rhaetian, while deeper zones belonging to the Rhaetian yield only minor contributions to water productivity. Main inflows have been recorded within the karstified section between 15.0 and 20.0 m and at depths listed in Table 4, as a result of fluid logging. However, at first glance, there is no

Table 8 Main results for the different water samples represented and explained in Fig. 14

Sample	1	2	3	4	5	6	7	8	9
PH	7.2	7.2	7.2	7.3	7.5	8.3	8.0	–	–
EC (µS/cm)	1,450	1,450	1,470	1,490	1,100	57,300	1,410	–	–
Na^+ (mg/l)	80.8	84.7	80.6	69.9	39.1	12100	96.8	77.7	36.4
K^+ (mg/l)	3.22	3.16	3.00	2.48	2.62	436	2.87	2.98	2.61
Mg^{2+} (mg/l)	36.4	34.8	39.8	44.6	51.0	1490	33.3	39.5	51.8
Ca^{2+} (mg/l)	127	128	127	165	112	462	140	136	111
Cl^- (mg/l)	192	203	206	181	77.0	20,800	206	195	71.0
SO_4^{2-} (mg/l)	77.5	77.3	81.4	84.5	180	3040	87.0	79.5	185
NO_3^- (mg/l)	46.3	39.8	37.1	40.4	8.00	bdl	37.4	41.1	6.70
HCO_3^- (mg/l)	531	488	470	537	384	183	378	516	384
SR_B (µg/l)	10.2	25	40	15	11	bdl	250	bdl	bdl

EC electrical conductivity; *SR_B* Sulphorhodamine B, *bdl* below detection limit
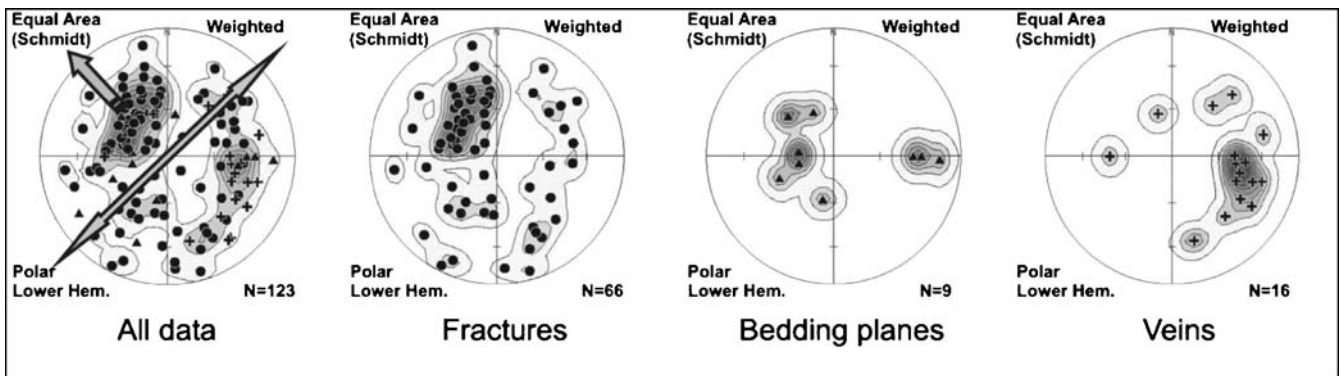
Fig. 15 Spatial orientation of structural features, the normal vectors of structural planes are projected onto the lower hemisphere (*Polar Lower Hem.*) using an equal area projection (or Schmidt stereographic net)

correlation between flow zone and spatial distribution, orientation and type of the recognised fractures, veins and bedding planes. For example, observed flow zones at 27.15 and at 29.54 m can be related to fractures, but fracture density is very low within this section and neither fracture type nor distribution possess significant characteristics compared to other depths. On the other hand, at 47.2 m an easy detectable planar fracture occurs which produces a major inflow, but similar fractures are abundant within this zone yielding no water. Furthermore, fracture density seems to be much higher at 42.0 m, where no flow zone is present (Fig. 5).

In order to test possible correlation between flow zones and structural geological features, the concept of flow through fracture intersections is tested. This concept postulates that water flows predominantly along intersection lines of certain fractures (pipe flow) rather than on singular fracture surfaces (planar flow). If the borehole or its surrounding skin zone cuts such an intersection line, water enters the well and a flow zone will occur at that depth. On the other hand, if an intersection line is missed by a certain distance, it will not be "seen" from the borehole and no flow zone will appear, even if flow occurs on that intersection line. In order to test this concept on this

dataset, a routine was written. This routine calculates strike, dip and location of all possible intersection lines of the recognised fractures. Finally, the shortest distances
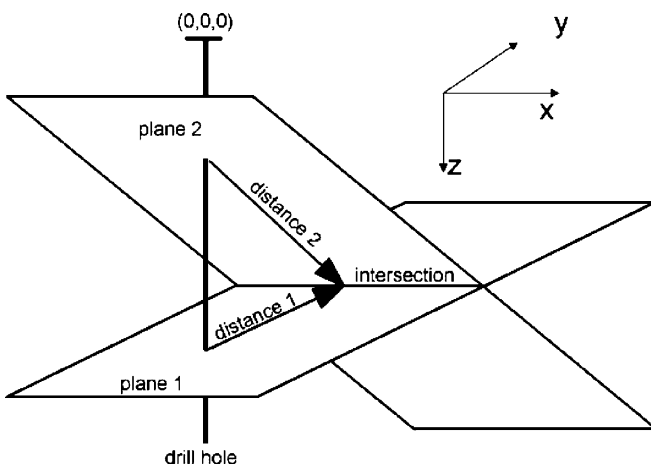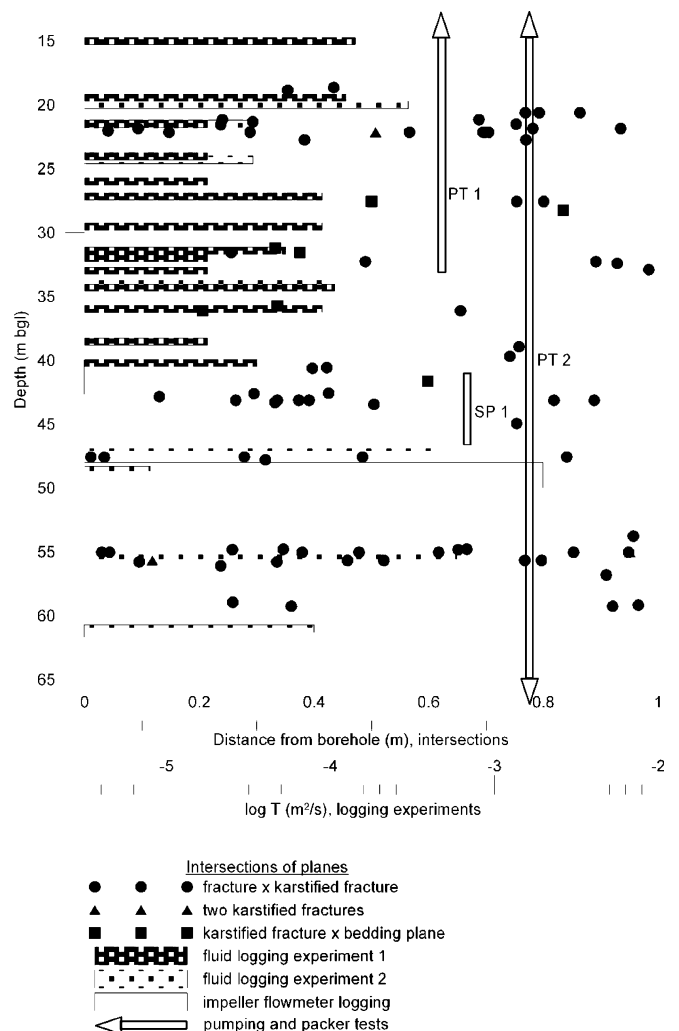

Fig. 17 Results from the fracture analysis in relation to the results from the hydraulic experiments. The main flowing features—high transmissivity (*T*)—correlate well with the levels where at least one of the intersecting features is karstified. This correlation diminishes with distance of the intersection to the borehole wall

Fig. 16 Conceptual model for calculating intersection lines of fractures

between the borehole and the intersection lines, measured along both involved fractures, are calculated (Fig. 16). Based on 123 fractures, veins and bedding planes, a total number of 7,503 intersection lines and 15,006 distance vectors were calculated. Only intersections at a distance of maximum 1 m are considered as relevant, resulting in 503 distance vectors pointing to 304 intersection lines. The data are grouped according to type of involved planes (bedding planes, veins, fractures, karstification) and displayed as distance versus depth graphs. If at least one of the involved fractures is karstified, a meaningful plot results. Figure 17 shows the corresponding plot together with the location of flow zones determined by fluid hydrochemical and impeller flowmeter logging. This interpretation confirms the three main inflow points at 21.5, 47.2 and 55.5 m as the intersection of karstified fractures at distances of less than 10 cm from the borehole. For distances larger than 10 cm, the correlation seems to be quite good as well; however, scattering of the data points gets larger, and additional data points emerge at depths where no flow zones could be detected. This concept is very promising for prediction of flow zones in fractured and karstified rock, but its general validity still has to be tested on other datasets.

Conclusion

This paper presents an integrated approach combining geophysical with several hydraulic testing methods during drilling. This approach was designed to identify and quantify the main flow zones in a fractured karstified environment and to link these to a geological meaningful explanation.

A first conclusion concerns the overall consistency of the results. The total transmissivity derived from the two open-hole pumping tests agrees with the total transmissivity derived from the trial and error fitting of the fluid-logging experiment (within the same order of magnitude). The transmissivity resulting from the impeller flowmeter is also within the same order of magnitude. All the hydraulic testing confirms the result from core analysis, that the Lias upper part is more transmissive than the lower Rhaetian part. More precise information on the flowing paths within the formations is gathered from fluid logging and impeller flowmeter, the former clearly indicating flow points, whereas the flowmeter only indicates flow zones. Fluid logging also allows a ranking of more and less transmissive features.

A careful description of core characteristics and the borehole wall images divides the aquifer in the MP1 borehole into two distinct intervals: an upper Lias part with mostly fractured and karstified limestone, and a lower Rhaetian zone with alternating beds of dolomite and clayey siltstones, with a small transition zone separating the two.

However, the most important results come from combining the hydraulic and geological description. The hypothesis postulated in the discussion stipulates that flow zones can be correlated to intersecting features of which at least one is karstified and where the intersection is less than 10 cm away from the borehole axis. The data set used in this work is too small to generate a truly general conclusion, but may be helpful in distinguishing which fractures, veins or beds could qualify as important for flow between many more that appear to have no influence on flow.

Continuous sampling of formation water and back-calculation of the formation concentration by taking the amount of mixed drilling fluid into account shows that the water in the Rhaetian part of the aquifer has higher sulphate content and differs from water in the upper part of the aquifer. The electrical conductivity profiles recorded after flushing the borehole clearly identify the presence of ambient flow. This phenomenon, along with the marked contrast in geochemical composition of the upper and lower part of the aquifer, may in part explain the change in quality over time in some regional observation wells. These, as mentioned in the introduction, have slotted screens over the entire Lias–Rhaetian aquifer.

References

Aeschbach-Hertig W et al (1998) A 3H/3He study of ground water flow in a fractured bedrock aquifer. Ground Water 36 (4):661

Arfib B, de MG, Ganoulis J (2000) Pollution by seawater intrusion into a karst system: new research in the case of the Almyros Source (Heraklio, Crete, Greece). In: S Lojen, H Doctor Daniel, AR Byrne (eds) Papers presented at the International workshop "Groundwater pollution in karst: preserving water quality in karst systems". Slovenska Akademija Znanosti in Umetnosti, Ljubljana, Slovenia

Barón Períz A, González Casasnovas C (1987) Hidrogeología de la isla de Mallorca, IV [Hydrogeology of Mallorca]. Simposio de Hidrogeología. Servicio Hidráulico de Baleares, Palma de Mallorca, 82 pp

Cardoso da Silva Junior G (1997) Comportamiento de los manatiales dels karst nororiental de la Serra de Tramuntana, Mallorca [Behaviour of the northeastern karst springs of the Serra de Tramuntana, Mallorca]. PhD Thesis, Universitat Poltècnica de Catalunya, Barcelona

Custodio E, Bayó A, Pascual M, Bosch X (1991) Results from studies in several karst formations in southern Catalonia (Spain). In: G Gunay, AI Johnson, W Back (eds) Hydrogeological processes in karst terranes. IAHS-AISH Publication. International Association of Hydrological Sciences, Louvain, pp 295–326

Gelabert B (1997) La estructura geológico de la mitad occidental de la isla de Mallorca [Geological structure of the western half of Mallorca]. Memoria del Instituto Tecnologico Geominero de España Thesis, Universidad Politécnica de Cataluña, Barcelona, p 129

Gelabert B et al (1996) Nuevas perspectivas sobre la unidad hidrogeológico de S'Almadrava, Serra de Tramuntana (Mallorca): interpretación de datos químicos e isotópicos basada en estodios geológicos [New insights into the hydrogeological unit of S'Almadrava, Serra de Tramuntana (Mallorca)]. Conference Proceedings Recursos Hidricos en Regiones Karsticos, Conference Proceedings, Vitoria-Gasteiz, Spain, pp 201–216

González Casasnovas C, López García JM, Mateos Ruíz RM (2000) El estado de las aguas subterráneas en el archipiélago Balear: Isla de Mallorca [The current state of groundwater in Balearic islands: the island of Mallorca]. Govern de les Illes Baleares. Conselleria de Medi Ambient-Eptisa, Palma de Mallorca

Hale FV, Tsang CF (1988) A code to compute borehole fluid conductivity profiles with multiple feed points. NAGRA, pp 88–21

Hearst JR, Nelson PH, Paillet FL (2000) Well logging for physical properties: a handbook for geophysicists, geologists and engineers. Wiley, Chichester, p 483

Hoehn E et al (1998) The Grimsel migration experiment: field injection-withdrawal experiments in fractured rock with sorbing tracers. J Contam Hydrol 34(1–2):85

Karasaki K (1990) A systematized drillstem test. Water Resour Res 26(12):2913

López García JM (1999) Cartografía geológica a escala 1:25.000 del sector Pollensa-Bahía de Pollensa (Mallorca) [Geological map at a scale of 1:25000 for the part of Pollensa-Pollensa Bay (Mallorca)], Palma de Mallorca

Milnes E, Renard P (2004) The problem of salt recycling and seawater intrusion in coastal irrigated plains: an example from the Kiti aquifer (southern Cyprus). J Hydrol 288(1–4): 327–343

Paillet FL (1993) Using borehole geophysics and cross-borehole flow testing to define hydraulic connections between fracture zones in bedrock aquifers. J Appl Geophys 30(4):261

Paillet FL (1995) Using Borehole flow logging to optimise hydraulic test procedures in heterogeneous fractured aquifers. Hydrogeol J 3(3):4–20

Parra JO, Hackert CL, Xu PC (2002) Characterization of fractured low Q zones at the Buena Vista Hills reservoir, California. Geophysics 67(4):1061

Petalas CP, Diamantis IB (1999) Origin and distribution of saline groundwaters in the upper Miocene aquifer system, coastal Rhodope area, northeastern Greece. Hydrogeol J 7(3):305–316

Sanz E et al (2002) Modelling coastal salty springs: first approach in carbonate media (S'Almadrava, Mayorca, Spain). In: Boekelman RH et al (eds) 17th Salt Water Intrusion Meeting (SWIM17). Delft University of Technology, Delft, The Netherlands, pp 195–203

Schnegg PA, Doerfliger N (1997) An inexpensive flow-through field fluorometer. 6th Conference on Limestone Hydrology and Fissured Media, Conference proceedings, La Chaux-de-Fonds, Switzerland, pp 47–50

Skinner D, Heinson G (2004) A comparison of electrical and electromagnetic methods for the detection of hydraulic pathways in a fractured rock aquifer, Clare Valley, South Australia. Hydrogeol J 12(5):576–590

Tsang C-F, Hufschmied P (1988) A borehole fluid conductivity logging method for the determination of fracture inflow parameters. Nagra, Baden, Switzerland, pp 88–13

Tsang CF, Hufschmied P, Hale FV (1990) Determination of fracture inflow parameters with a borehole fluid conductivity logging method. Water Resour Res 26(4):561–578

Tulipano L, Fidelibus MD (1996) Multitracing approach for the identification of main hydrogeological pathways feeding coastal springs of karstic aquifer. In: Buddemeier RW (ed) Groundwater discharge in the coastal zone: proceedings of an international symposium held at the Russian Academy of Sciences. LOICZ Reports and Studies. LOICZ Core Project, Netherlands Institute for Sea Research, Texel, Netherlands, pp 113–121

Zanini L et al (2000) Ground water flow in a fractured carbonate aquifer inferred from combined hydrogeological and geochemical measurements. Ground Water 38(3):350